**PAPER**

# Investigation of anisotropic mechanical, electronic, and charge carrier transport properties of germanium-pnictogen monolayers

To cite this article: M Abboud *et al* 2022 *J. Phys. D: Appl. Phys.* **55** 185302

View the article online for updates and enhancements.

# Investigation of anisotropic mechanical, electronic, and charge carrier transport properties of germanium-pnictogen monolayers

**M Abboud**[1] , **D H Ozbey**[1] , **M E Kilic**[2] **and E Durgun**[1],*

[1] UNAM—National Nanotechnology Research Center and Institute of Materials Science and Nanotechnology, Bilkent University, Ankara 06800, Turkey
[2] Computational Science Research Center, Korea Institute of Science and Technology, Seoul 02792, Republic of Korea

E-mail: durgun@unam.bilkent.edu.tr

CrossMark

## Abstract

Recently, novel two-dimensional (2D) GeP and GeAs systems have been fabricated by mechanical exfoliation and utilized in various applications. These developments have brought the 2D germanium-pnictogens, C2/m-Ge$X$ ($X$ = N, P, As, Sb, and Bi) structures into the limelight. In this study, we systematically investigate the structural, mechanical, electronic, and charge carrier transport properties of Ge$X$ monolayers by using first-principles methods. Our results show that the considered systems are dynamically stable and possess anisotropic physical properties. Examined structures are found to be flexible, and their mechanical strength and stiffness decrease down the group-V, in line with the trends of the bond strength, cohesive energy, charge transfer, and electron localization function. Additionally, the zigzag in-plane direction is mechanically superior to the armchair direction. The electronic band structure calculations based on HSE06 hybrid functional with the inclusion of spin–orbit coupling indicate that Ge$X$ monolayers are either direct or quasi-direct semiconductors with band gaps lying within the infrared and visible spectrum. The estimated charge carrier mobilities are highly anisotropic and also differ significantly depending on the structure and carrier type. These unique properties render Ge$X$ monolayers as suitable 2D materials for flexible nanoelectronic applications.

Supplementary material for this article is available online

(Some figures may appear in colour only in the online journal)

---

* Author to whom any correspondence should be addressed.

# 1. Introduction

Pioneered by the realization of free-standing graphene [1], the field of two-dimensional (2D) materials has started to grow rapidly followed by isolation of mono- or few-layer crystals from their layered bulk form [2, 3]. Mechanical exfoliation is one of the widely used and succeeding methods to obtain high-quality 2D systems [4]. In this framework, the recent synthesis of layered single-crystals of silicon and germanium monopnictides by using the high-pressure melt growth technique [5] implies the possible realization of 2D group IV–V structures. The produced bulk systems belong to the monoclinic C2/m symmetry and have weak interlayer interactions with exfoliation energies comparable to that of graphite [6–8]. Later, 2D GeP and GeAs have been exfoliated from their bulk precursors by mechanical and liquid-phase exfoliation methods, respectively [9, 10]. These enabled several experimental studies on these systems to explore their thickness-dependent optical, electrical, and thermoelectric properties [6, 9–14].

Following their successful fabrications, 2D forms of the group IV–V structures have been used in several applications. For instance, GeP flakes have been employed in lithium- and sodium-ion batteries and proven to undergo unique Li- and Na-reaction phase-change mechanisms, rendering them an alternative anode material for high-capacity batteries [15–17]. 2D GeAs has been exploited as an ultra-thin channel material in field-effect transistors with a high p-type electrical conductivity, and tunable field-effect mobility [18, 19]. GeAs nanosheets have also been utilized in photodetectors functioning in the infrared and visible domain [10, 20]. The fabricated group IV–V structures possess highly anisotropic physical properties [6, 21, 22] due to the presence of different types of bonds along armchair and zigzag in-plane directions [23]. Furthermore, theoretical studies have revealed that group IV–V monolayers are excellent ultraviolet and visible light absorbers, rendering them as potential materials for photovoltaic and solar cell devices [6, 24–26]. Other studies have demonstrated that they possess desirable photocatalytic characteristics, which are useful in solar water splitting applications [21, 27–34]. Moreover, their strong optical absorption in ultraviolet and visible light ranges suggests that they are promising candidate materials for optoelectronic applications [6]. Additionally, it has been shown that the physical properties of 2D group IV–V structures are tunable via doping and strain engineering [6, 22, 23, 35].

Although numerous theoretical studies have focused on GeP and GeAs crystals among 2D Ge-pnictogens, other members of the class have not been examined thoroughly. Motivated by the realization of 2D group IV–V systems in C2/m symmetry [5, 9, 10], and their novel properties, in this paper, we extensively examined C2/m-Ge*X* (*X* = N, P, As, Sb, and Bi) monolayers. Firstly, we reveal the stability of the considered 2D crystals and then systematically investigate their structural, mechanical, and electronic characteristics. Giving particular attention to electronic transport properties, highly accurate calculations have been performed to estimate the effective mass and mobility of charge carriers.

# 2. Method

In this study, we used the Vienna *Ab initio* Simulation Package [36–39] to perform first-principle calculations based on density functional theory with project-augmented wave potentials [40]. Perdew–Burke–Ernzerhof (PBE) functional within the generalized gradient approximation (GGA) was considered for the exchange-correlation potential. Heyd–Scuseria–Ernzerhof (HSE06) hybrid functional was adopted to correct the underestimated band gap values obtained at GGA-PBE level [41, 42]. Van der Waals interactions were described based on the Grimme method [43]. The spin–orbit coupling (SOC) were taken into account in the electronic structure calculations. The cutoff energy was set to 530 eV, and a vacuum space of 20 Å was placed along the non-periodic axis to prevent any artificial interactions. The Brillouin zone was sampled uniformly by a $12 \times 2 \times 1$ k-point mesh based on the Monkhorst–Pack scheme [44]. Electronic and ionic step convergence criteria were set to $10^{-5}$ and $10^{-4}$ eV, respectively. *Ab initio* molecular dynamics (AIMD) simulations were performed for supercells dimensions of $\sim16$ Å $\times$ 16 Å to nullify the size constraint. The AIMD simulations were performed using a microcanonical ensemble by scaling the atomic velocities at 300, 600, and 900 K for 3 ps total simulation with 1 fs time steps. Bader charge analysis [45] was utilized to evaluate the charge transfer between the atoms. The cohesive energy per atom ($E_c$) was calculated as follows:

$$E_c = \frac{E_{\text{Ge}X} - (N_{\text{Ge}} \times E_{\text{Ge}}) - (N_X \times E_X)}{N_{\text{Ge}} + N_X} \quad (1)$$

where $E_{\text{Ge}X}$ is the total energy of C2/m-Ge*X* monolayer; $E_{\text{Ge}}$ ($E_X$) is the energy of a single germanium (pnictogen) atom; and $N_{\text{Ge}}$ ($N_X$) is the number of germanium (pnictogen) atoms per unit cell.

To probe the mechanical properties of the structures, tensile and compression tests were performed by applying uniaxial strain until the fracture point. Stress values were calculated as $\sigma = \frac{1}{A_0} \frac{\partial E}{\partial \epsilon}$, where $A_0$ is the area of unit cell, and $\epsilon$ is the applied strain ($\epsilon = (l - l_0)/l_0$, where $l$ and $l_0$ are the strained and pristine cell dimensions, respectively). The structure was relaxed at each strain step to ensure that there was no external pressure or internal stresses. Toughness ($U$) was calculated as the total area under the stress–strain curve. Elastic tensor was computed with high accuracy to obtain the elastic constants, and deduce the angle-dependent in-plane stiffness ($Y_{2D}$) and Poisson's ratio ($\nu$).

# 3. Results and discussion

## 3.1. Structural properties and stability

The pristine structure of a typical C2/m-Ge*X* monolayer is shown in figure 1 where the unit cell containing 12 Ge-atoms and 12 *X*-atoms (*X* = N, P, As, Sb, and Bi) is marked by

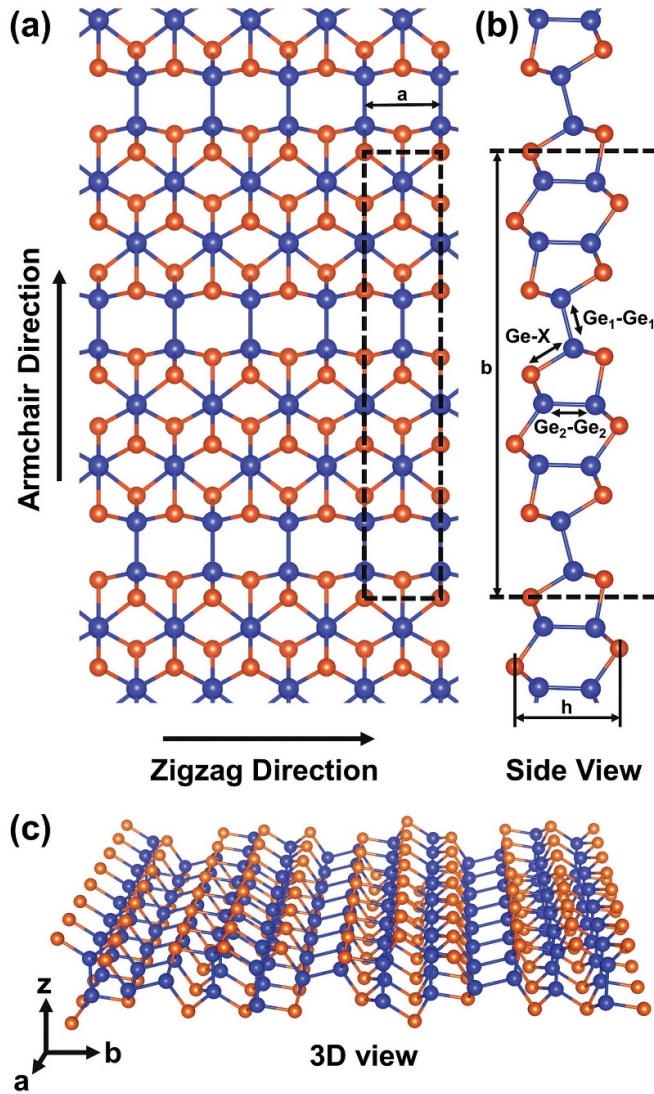J. Phys. D: Appl. Phys. **55** (2022) 185302

M Abboud *et al*



**Figure 1.** (a) Top, (b) side, and (c) 3D views of a representative GeX monolayer in the C2/m space group. The unit cell is marked by dashed lines. Three different types of bonds (Ge$_1$−Ge$_1$, Ge$_2$−Ge$_2$, and Ge-X), lattice constants (**a** and **b**), and thickness (**h**) are labeled.



**Figure 2.** The variation of zigzag lattice constant (**a**), the armchair lattice constant (**b**), layer thickness (**h**), and cohesive energy ($E_c$) with type of the C2/m-GeX monolayers.

dashed lines and projected onto the top and side views of the monolayer. The unit cell is identical to traditionally considered unit cells for group IV–V monolayers in the C2/m phase [5, 6, 21, 22, 33]. The armchair (ac) lattice parameter **b** is around six times larger than the zigzag (zz) lattice parameter **a**, giving C2/m-GeX monolayers a high degree of asymmetry. The lattice parameters (**a** and **b**) and thickness **h** are found to increase as the size of the X-atom enlarges from N to Bi. Three types of bonds (Ge$_1$−Ge$_1$, Ge$_2$−Ge$_2$, and Ge-X) can be identified in these configurations and are all labeled on the side view of figure 1. The bond lengths d$_{Ge_1−Ge_1}$ and d$_{Ge_2−Ge_2}$ are almost constant for all the structures, while d$_{GeX}$ increases down the X-group. The variations of the structural parameters together with $E_c$ as a function of elemental composition are presented in figure 2 and table 1.

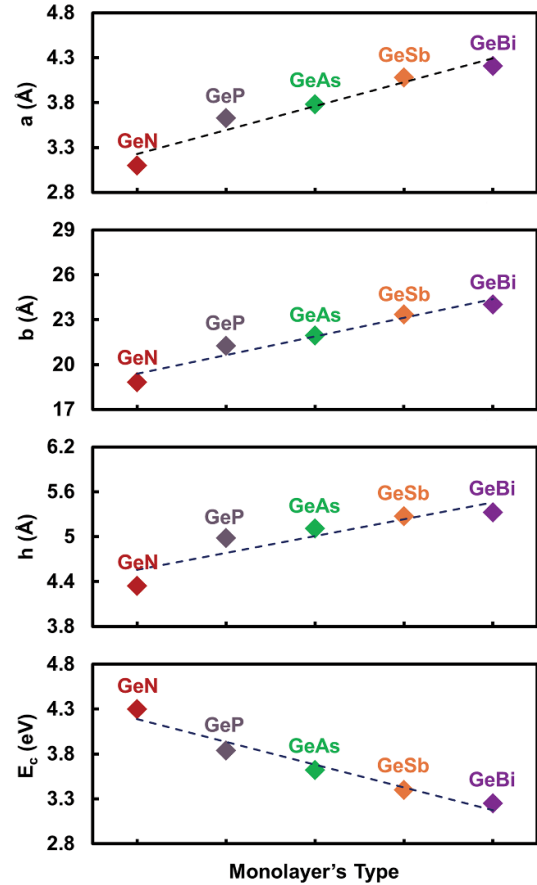Bader charge analysis shows that, while the net atomic charge on Ge-atoms increases from 2.66 to 4.08 e$^−$, that of the X-atoms decreases from 6.30 to 4.92 e$^−$ down the X-group. Accordingly, charge transfer ($\Delta\rho$) from Ge to X atoms reduces from −1.34 to −0.30 until GeAs, and it becomes very small for GeSb and GeBi. These results are consistent with the electronegativity difference between the considered atoms. N, P, and As atoms have a higher electronegativity than Ge, while Sb, Bi, and Ge are very close to each other. In conjunction with the decrease in $\Delta\rho$, $E_c$ reduces with a similar trend. However, $E_c$'s are relatively high for all the structures (3.25–4.30 eV) and indicate strong covalent bonding. The calculated $E_c$ values for C2/m-GeX are comparable to those reported for P$\bar{3}$m1 and P$\bar{6}$m2 phases [46, 47], revealing that $E_c$ does not vary with the group symmetry of C2/m-GeX but depends more on the type of the constituent elements.

To confirm the stability of the structures, AIMD simulations for large enough supercells (minimum of 16 Å × 16 Å) for 3 ps is performed. Figure 3 shows the fluctuation of total energy (E$_{fluct}$) during the AIMD simulations and the snapshots of C2/m-GeX at 300 K. E$_{fluct}$ is found to be below 1% and the deformation in the structures is minimal. Similar results are also obtained for 600 and 900 K (see supporting information available online at stacks.iop.org/JPhysD/55/185302/mmedia), revealing the dynamical stability of all the structures at room temperature and above.

J. Phys. D: Appl. Phys. **55** (2022) 185302

M Abboud *et al*

**Table 1.** The structural properties of C2/m-Ge*X* monolayers. The zigzag lattice constant (**a**), armchair lattice constant (**b**), layer thickness (**h**), bond lengths (d), cohesive energy ($E_c$), and Bader atomic charges on Ge and *X* atoms ($\rho_{(Ge)}$, $\rho_{(X)}$), and charge difference ($\Delta\rho$).

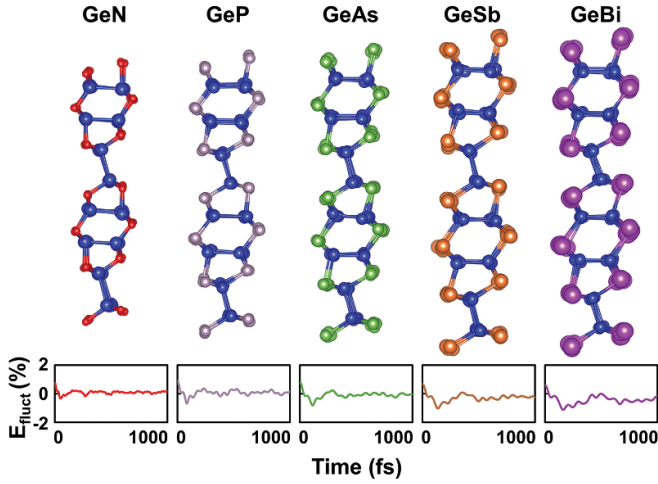| Structure | **a** (Å) | **b** (Å) | **h** (Å) | $d_{Ge_1-Ge_1}$ (Å) | $d_{Ge_2-Ge_2}$ (Å) | $d_{GeX}$ (Å) | $E_c$ (eV atom$^{-1}$) | $\rho_{(Ge)}$ (e$^-$) | $\rho_{(X)}$ (e$^-$) | $\Delta\rho$ (e$^-$) |
|---|---|---|---|---|---|---|---|---|---|---|
| GeN | 3.10 | 18.82 | 4.34 | 2.46 | 2.48 | 1.94 | 4.30 | 2.66 | 6.34 | −1.34 |
| GeP | 3.63 | 21.25 | 4.98 | 2.46 | 2.48 | 2.37 | 3.84 | 3.50 | 5.50 | −0.50 |
| GeAs | 3.78 | 21.96 | 5.11 | 2.47 | 2.48 | 2.48 | 3.62 | 3.70 | 5.30 | −0.30 |
| GeSb | 4.08 | 23.35 | 5.27 | 2.47 | 2.48 | 2.68 | 3.40 | 4.04 | 4.96 | +0.04 |
| GeBi | 4.21 | 24.03 | 5.33 | 2.47 | 2.48 | 2.76 | 3.25 | 4.08 | 4.92 | +0.08 |



**Figure 3.** The fluctuation of total energy during the AIMD simulations and the side view snapshots of the C2/m-Ge*X* monolayers after 1000 MD steps at 300 K.



**Figure 4.** Angle-dependent variation of (a) the in-plane stiffness ($Y_{2D}(\theta)$) and (b) the Poisson's ratio ($\nu(\theta)$) of C2/m-Ge*X* monolayers. Inset shows the angle ($\theta$) with respect to C2/m structure.

### 3.2. Mechanical properties

Revealing the stability of C2/m-Ge*X* monolayers, the mechanical properties are examined. Firstly, the elastic tensor is computed to obtain the elastic constants ($C_{ij}$) of each structure. $C_{ij}$ are then used to calculate the angle-dependent in-plane stiffness ($Y_{2D}(\theta)$) and Poisson's ratio ($\nu(\theta)$) according to the following formulas [48],

$$Y_{2D}(\theta) = \frac{(C_{11}C_{22} - C_{12}^2)}{C_{11}s^4 + C_{22}c^4 + \left(\dfrac{C_{11}C_{22} - C_{12}^2}{C_{66}} - 2\,C_{12}\right)c^2s^2} \tag{2}$$

$$\nu(\theta) = -\frac{\left(C_{11} + C_{22} - \dfrac{C_{11}C_{22} - C_{12}^2}{C_{66}}\right)c^2s^2 - C_{12}(c^4 + s^4)}{C_{11}s^4 + C_{22}c^4 + \left(\dfrac{C_{11}C_{22} - C_{12}^2}{C_{66}} - 2\,C_{12}\right)c^2s^2} \tag{3}$$

where $s = \sin(\theta)$ and $c = \cos(\theta)$.

The orientation dependence of $Y_{2D}$ and $\nu$ is shown in figures 4(a) and (b), where the zigzag and amrchair directions are positioned at 0° and 90°, respectively. As can be seen in figure 4(a), $Y_{2D}(\theta)$ peaks at 0° and decreases gradually
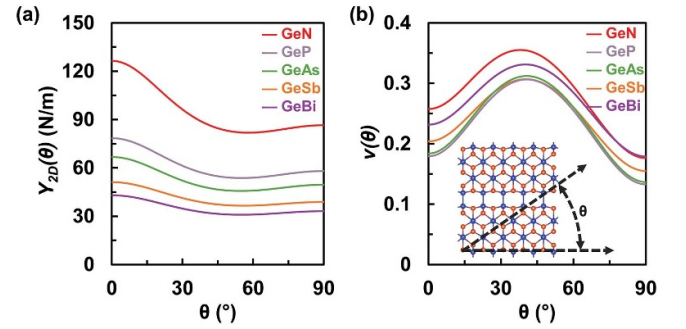
toward 90°, indicating that the structures are stiffer along zigzag direction than armchair direction. GeN is found to be the most rigid system among C2/m-Ge*X* monolayers ($Y_{2D}^{ac} = 87$ and $Y_{2D}^{zz} = 126$ N m$^{-1}$, which are comparable to that of MoS$_2$ [49]). $Y_{2D}$ decreases down the *X*-group in accordance with the variation of $E_C$ and $\Delta\rho$. Accordingly, the rest of C2/m-Ge*X* crystals are soft and their stiffness is comparable to that of silicene [50, 51]. $\nu(\theta)$ peaks at ∼45°, and similar to $Y_{2D}$, $\nu^{zz}$ is larger than $\nu^{ac}$. $\nu$ is within the same range as MoS$_2$ and silicene [52].

To obtain other fundamental mechanical properties, namely ultimate tensile strength ($\sigma_T$), ultimate compressive strength ($\sigma_C$), tensile toughness ($U_T$), compressive toughness ($U_C$), maximum tensile strain ($\epsilon_T$), and maximum compressive strain ($\epsilon_C$), a uniaxial strain ($\epsilon^{zz}$ and $\epsilon^{ac}$) is applied along the zigzag and armchair directions, separately. The strain step size of 0.1 Å is considered, and the structures are relaxed at each step, and the attained results are listed in table 2. The mechanical response of C2/m-Ge*X* monolayers beyond the elastic regime is also found to be anisotropic, and the strength and toughness decrease expectedly down the *X*-group. It is worth mentioning that the mechanical properties in the zigzag direction are superior to those in the armchair direction for all the structures. The main reason for the anisotropic behavior is the presence of the Ge$_1$−Ge$_1$ bonds (shown in figure 1) which not only have a lower bond order than the rest of the bonds but also are stress concentration sites which limit the structure's ability to withstand stress along the armchair direction [23]. When compared, the tensile strength values of Ge*X* monolayers, are lower than those of graphene

**Table 2.** Mechanical properties C2/m-Ge*X* monolayers. Ultimate tensile strength ($\sigma_T$), ultimate compressive strength ($\sigma_C$), tensile toughness ($U_T$), compressive toughness ($U_C$), maximum tensile strain ($\epsilon_T$), maximum compressive strain ($\epsilon_C$), Poisson's ratio ($\nu$), and in-plane stiffness ($Y_{2D}$).

| Direction | Structure | $\sigma_T$ (N m$^{-1}$) | $\sigma_C$ (N m$^{-1}$) | $U_T$ (N m$^{-1}$) | $U_C$ (N m$^{-1}$) | $\epsilon_T$ (—) | $\epsilon_C$ (—) | $\nu$ (—) | $Y_{2D}$ (N m$^{-1}$) |
|---|---|---|---|---|---|---|---|---|---|
| Zigzag | GeN | 10.20 | 32.75 | 2.40 | 4.77 | 0.26 | −0.23 | 0.26 | 126.4 |
|  | GeP | 6.51 | 11.38 | 2.02 | 1.27 | 0.30 | −0.17 | 0.18 | 78.5 |
|  | GeAs | 5.41 | 8.38 | 1.80 | 0.95 | 0.32 | −0.16 | 0.18 | 66.9 |
|  | GeSb | 4.03 | 4.44 | 1.08 | 0.68 | 0.29 | −0.20 | 0.20 | 51.2 |
|  | GeBi | 3.67 | 3.48 | 0.93 | 0.49 | 0.28 | −0.19 | 0.23 | 43.0 |
| Armchair | GeN | 4.66 | 6.45 | 0.76 | 1.04 | 0.19 | −0.13 | 0.18 | 86.5 |
|  | GeP | 3.75 | 5.63 | 0.63 | 0.77 | 0.19 | −0.17 | 0.13 | 58.1 |
|  | GeAs | 3.62 | 4.73 | 0.56 | 0.58 | 0.19 | −0.17 | 0.14 | 49.6 |
|  | GeSb | 3.42 | 3.56 | 0.51 | 0.29 | 0.19 | −0.14 | 0.15 | 38.9 |
|  | GeBi | 3.21 | 3.13 | 0.49 | 0.23 | 0.20 | −0.12 | 0.18 | 33.2 |

($\sigma_T^{ac} = 32.9\,\mathrm{N\,m^{-1}}$, $\sigma_T^{zz} = 36.2\,\mathrm{N\,m^{-1}}$) and h-BN ($\sigma_T^{ac} = 29.0\,\mathrm{N\,m^{-1}}$, $\sigma_T^{zz} = 33.7\,\mathrm{N\,m^{-1}}$) but more comparable to the strength of silicene ($\sigma_T^{ac} = 5.9\ \mathrm{N\,m^{-1}}$, $\sigma_T^{zz} = 6.0\ \mathrm{N\,m^{-1}}$) and borophene ($\sigma_T^{ac} = 10.0\,\mathrm{N\,m^{-1}}$, $\sigma_T^{zz} = 4.4\,\mathrm{N\,m^{-1}}$) [51, 53–55].

A more demonstrative way to visualize the effect of bonding on the mechanical properties is to analyze the electron localization function (ELF) in the structures [56]. Figure 5 illustrates the ELF profiles of the C2/m-Ge*X* monolayers. ELF = 1, represented in red, corresponds to perfect electron localization; ELF = 0.5, represented in green, refers to an electron-gas state; while any ELF value above 0.75 around the center of the bonds would indicate the existence of a covalent bonding [56–58]. As can be observed from figure 5, the localization of the electrons along the bonds decreases down the *X*-group, pointing out the weakening of the bonds. This is not only consistent with the electronegativity, charge transfer, and cohesive energy trends, but it also justifies the mechanical strength and stiffness values obtained. It is also worth noting that the asymmetric ELF profiles in the Ge-*X* bonds are due to the electronegativity difference between Ge and pnictogen atoms which leads to charge donation from Ge to *X*-atoms. For GeSb and GeBi, charge transfer is negligible, which in turn results in less electron localization within the monolayer while causing electrons to accumulate around the outer side of the *X*-atoms. This justifies the lower strength and higher flexibility of GeSb and GeBi monolayers. Our mechanical properties and ELF results of GeN, GeP, and GeAs are in agreement with the literature [22, 23].

### 3.3. Electronic properties

The electronic properties are investigated by computing the electronic band structures and the projected density of states (PDOS) of the C2/m-Ge*X* monolayers. The calculations are performed at the level of GGA-PBE and HSE06 by including SOC. Figure 6 shows the electronic band structures with the inset presenting the k-point path. To check the effect of SOC, the calculations are also performed without the SOC (see supporting information), and all the obtained band gaps ($E_g$) are
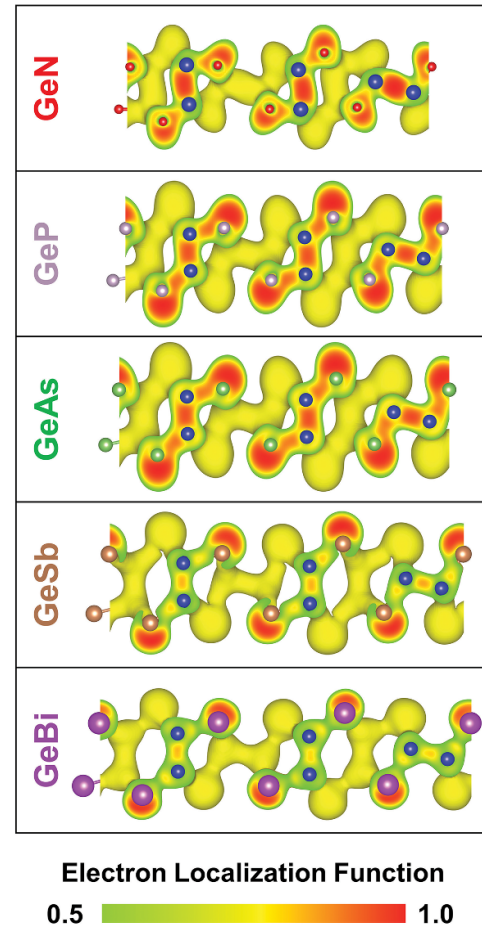


**Electron Localization Function**

0.5 ▬▬▬▬▬▬▬▬▬▬ 1.0

**Figure 5.** ELF overlaid onto the side views of C2/m-Ge*X* monolayers.

listed in table 3. The electronic band structures indicate that while GeN, GeP, and GeAs monolayers are quasi-direct (with ~30, ~60, and ~1 meV energy difference between direct and indirect band gap, respectively) GeSb and GeBi are direct band gap semiconductors. $E_g^{\mathrm{HSE-SOC}}$ of GeN (2.37 eV), GeP (2.35 eV) and GeAs (2.07 eV) lie within the visible spectrum
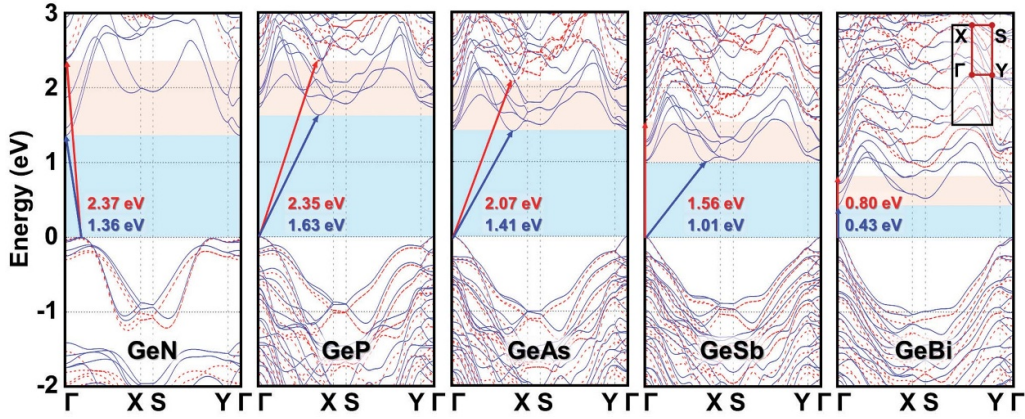
**Figure 6.** Electronic band structures of C2/m-Ge*X* monolayers. The GGA-PBE and HSE06 results are shown with blue solid and red dashed lines, respectively. The blue and red arrows mark the band gaps at the level of GGA-PBE and HSE06. The k-point path in the reciprocal space is given as an inset.

**Table 3.** The electronic band gaps of C2/m-Ge*X* monolayers calculated at the level of GGA-PBE and HSE06 with and without including SOC effects.

|  | $E_g^{\text{PBE}}$ (eV) | $E_g^{\text{HSE}}$ (eV) | $E_g^{\text{PBE}-\text{SOC}}$ (eV) | $E_g^{\text{HSE}-\text{SOC}}$ (eV) |
|---|---|---|---|---|
| GeN | 1.36 | 2.37 | 1.36 | 2.37 |
| GeP | 1.63 | 2.35 | 1.63 | 2.35 |
| GeAs | 1.45 | 2.11 | 1.41 | 2.07 |
| GeSb | 1.17 | 1.72 | 1.01 | 1.56 |
| GeBi | 0.78 | 1.25 | 0.43 | 0.80 |

and $E_g^{\text{HSE}-\text{SOC}}$ of GeSb (1.56 eV) and GeBi (0.80 eV) are in the infrared region and $E_g^{\text{HSE}-\text{SOC}}$ reduces down the *X*-group. This trend is related to the energy splitting between bonding and anti-bonding orbitals, which decreases with the increasing principal quantum number of the orbitals. As the Ge-N bonds are polar covalent (due large electronegativity difference between Ge and N atoms), the electronic structure of GeN is different from other C2/m-Ge*X* monolayers (figure 6). The results for GeP and GeAs monolayers are in agreement with the literature [6, 22, 30]. The inclusion of SOC results in band gap narrowing [59] and the effect becomes stronger as *X*-atom gets heavier. Consequently, while the band gap reduction is negligible for GeN and GeP, it is the largest (0.45 meV) for the GeBi monolayer.

In addition, the PDOS analysis shown in figure 7 indicated that the valence band maximum (VBM) originates from the hybridization of *p*-orbitals of both Ge- and *X*-atoms, where $p_z$-orbital is the most dominant in all cases. The conduction band minimum (CBM) originates from the hybridization of *s*-orbital of Ge and *p*-orbitals of *X*-atom, where *s*-orbital of Ge contributes the most in all structures except for the GeBi monolayer [6, 22, 23].

### 3.4. Charge carrier transport

As the new generation transistors have been miniaturized down to nanometer scale, together with noteworthy
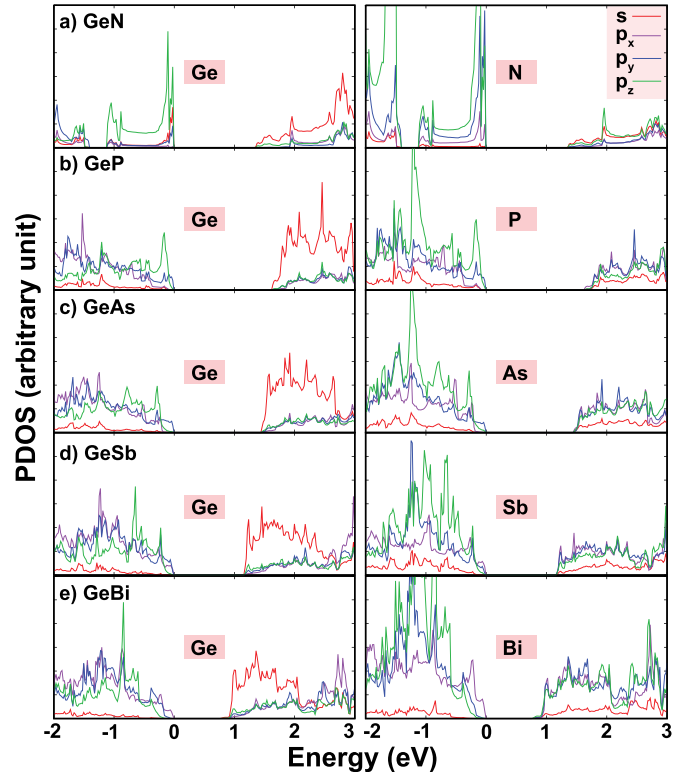


**Figure 7.** Atom and orbital PDOS of C2/m-Ge*X* monolayers.

advancements in *ab initio* methods, the theoretical search of appropriate 2D channel materials has accelerated [60]. Apart from the transistors, there is a great demand for 2D materials with diverse electronic conductance characteristics in various applications such as photocatalytic, optoelectronic, and photoelectric devices. Therefore, the theoretical specification of electronic transport properties of 2D semiconductors has become crucial. On the other hand, regarding the group IV–V monolayers, different values are reported in the literature [6, 28, 61]. This led us to investigate the effective mass and mobility of C2/m-Ge*X* monolayers with precise calculations to hinder accuracy issues. Deformation potential theory (DPT)
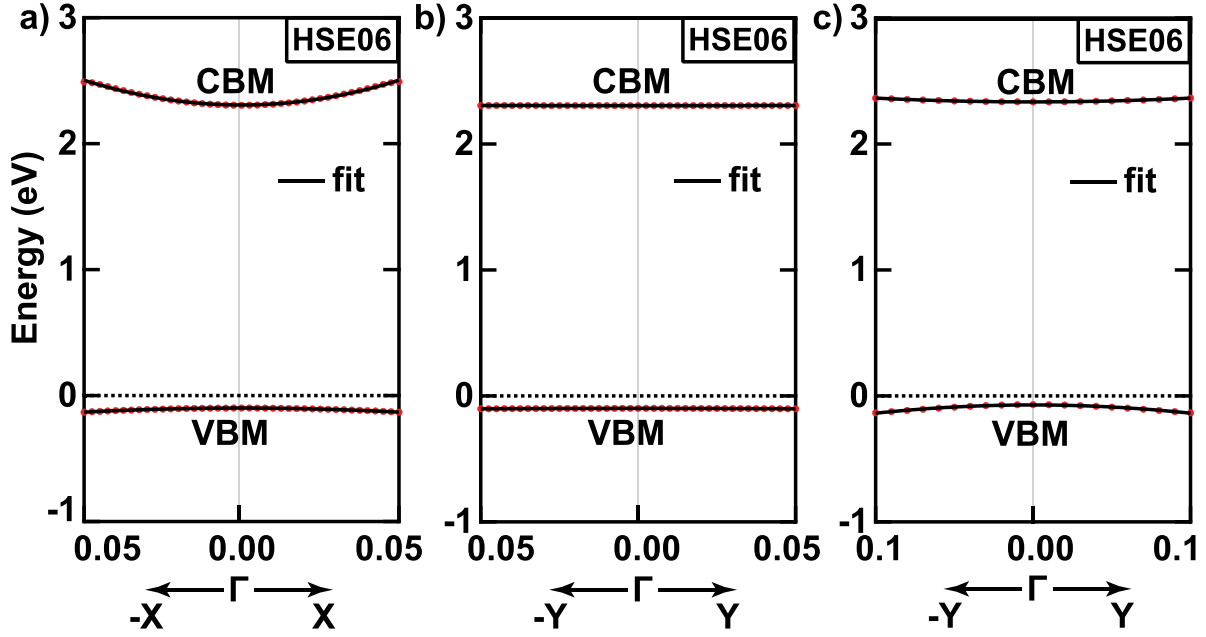
J. Phys. D: Appl. Phys. **55** (2022) 185302

M Abboud *et al*



**Figure 8.** Representative illustration of the effective mass calculation for (a) Γ-X (zigzag), (b) Γ-Y (armchair), and (c) Γ-Y directions with an extensive range in k-space.

**Table 4.** Carrier effective mass ($m^*/m_0$ where $m_0$ is the mass of free electrons) and mobility ($\mu$) of C2/m-Ge*X* monolayers along armchair (ac) and zigzag (zz) directions at room temperature T $=$ 300 K ($10^3$ cm$^2$ (V s)$^{-1}$).

|  | $m_{e,zz}^*$ | $m_{e,ac}^*$ | $m_{h,zz}^*$ | $m_{h,ac}^*$ | $\mu_{e,zz}$ | $\mu_{e,ac}$ | $\mu_{h,zz}$ | $\mu_{h,ac}$ |
|---|---|---|---|---|---|---|---|---|
| GeN | 0.07 | 1.75 | 0.47 | 2.61 | 10.90 | 11.40 | 1.22 | 0.18 |
| GeP | 0.05 | 4.54 | 0.29 | 1.70 | 154.85 | 0.01 | 72.25 | 0.02 |
| GeAs | 0.07 | 7.86 | 0.28 | 1.50 | 61.57 | 0.01 | 166.09 | 0.02 |
| GeSb | 0.07 | 4.07 | 0.20 | 3.75 | 169.11 | 0.01 | 0.07 | 0.19 |
| GeBi | 0.05 | 0.74 | 0.06 | 2.77 | 3.62 | 0.37 | 0.47 | 1.07 |

[62] and the conventional definition of effective mass [63] are exploited in this part of the work to maintain consistency with the earlier studies.

The effective mass, which is the main parameter of interest in obtaining the correct transport properties of semiconductors, is directly proportional to the inverse of the curvature of the electronic bands with the $m^* = \hbar \left( \frac{\partial E^2(\mathbf{k})}{\partial k^2} \right)^{-1}$ expression where $\hbar$ is the reduced Planck constant, and $\frac{\partial E^2(\mathbf{k})}{\partial k^2}$ is the second derivative of the energy with respect to $\mathbf{k}$, which denotes wave vector. Since dissimilar band dispersions throughout Γ-X (zigzag) and Γ-Y (armchair) directions indicate that all the group IV–V monolayers have anisotropic transport properties, the effective mass of holes ($m_{h,zz}^*$, $m_{h,ac}^*$) and electrons ($m_{e,zz}^*$, $m_{e,ac}^*$) are evaluated for both directions as shown representatively in figure 8. The band dispersion relation, E($\mathbf{k}$), is calculated in the vicinity of Γ point throughout 0.05 or 0.1 Å$^{-1}$ range in k-space. To avoid nonparabolic effects, k-point spacing of 0.0025–0.01 Å$^{-1}$ is considered. If the band dispersion deviates from parabolic behavior as seen in figure 8(b), a more extensive range (0.1 Å$^{-1}$) in reciprocal space is sampled with corresponding spacing as shown in figure 8(c). Even though HSE06 hybrid exchange-correlation functional does

not change electronic band profiles dramatically compared to GGA-PBE calculations, possible alterations are taken into account with hybrid functional to increase the accuracy of results. Thus, the effective mass of charge carriers is estimated accurately by fitting the second-order polynomial to the HSE06-calculated band dispersion. The results are summarized in table 4. It is found that $m_{e,zz}^*$ and $m_{h,zz}^*$ are significantly lower than $m_{e,ac}^*$ and $m_{h,ac}^*$ for all monolayers. Resultant values show that there is a strong anisotropy in carrier transport, which is consistent with the difference between electronic band dispersions along zigzag and armchair directions.

DPT is based on the fact that the atomic displacement resulting from a long-wavelength acoustic phonon deforms the crystal and modifies the electronic band dispersion, and can appropriately be employed to reflect the intrinsic charge-transport characteristics of semiconducting systems. Therefore, the deformation potential constant $E_d$ is calculated by giving small tensile and compressive strains (on the order of $10^{-3}$) along both directions to mimic the deformation of lattice caused by phonons. Energy shifts of VBM and CBM as a function of compressive and tensile strain for all monolayers can be seen in figure 9. The slopes of the straight lines (written in bold) obtained by linear fitting correspond to the
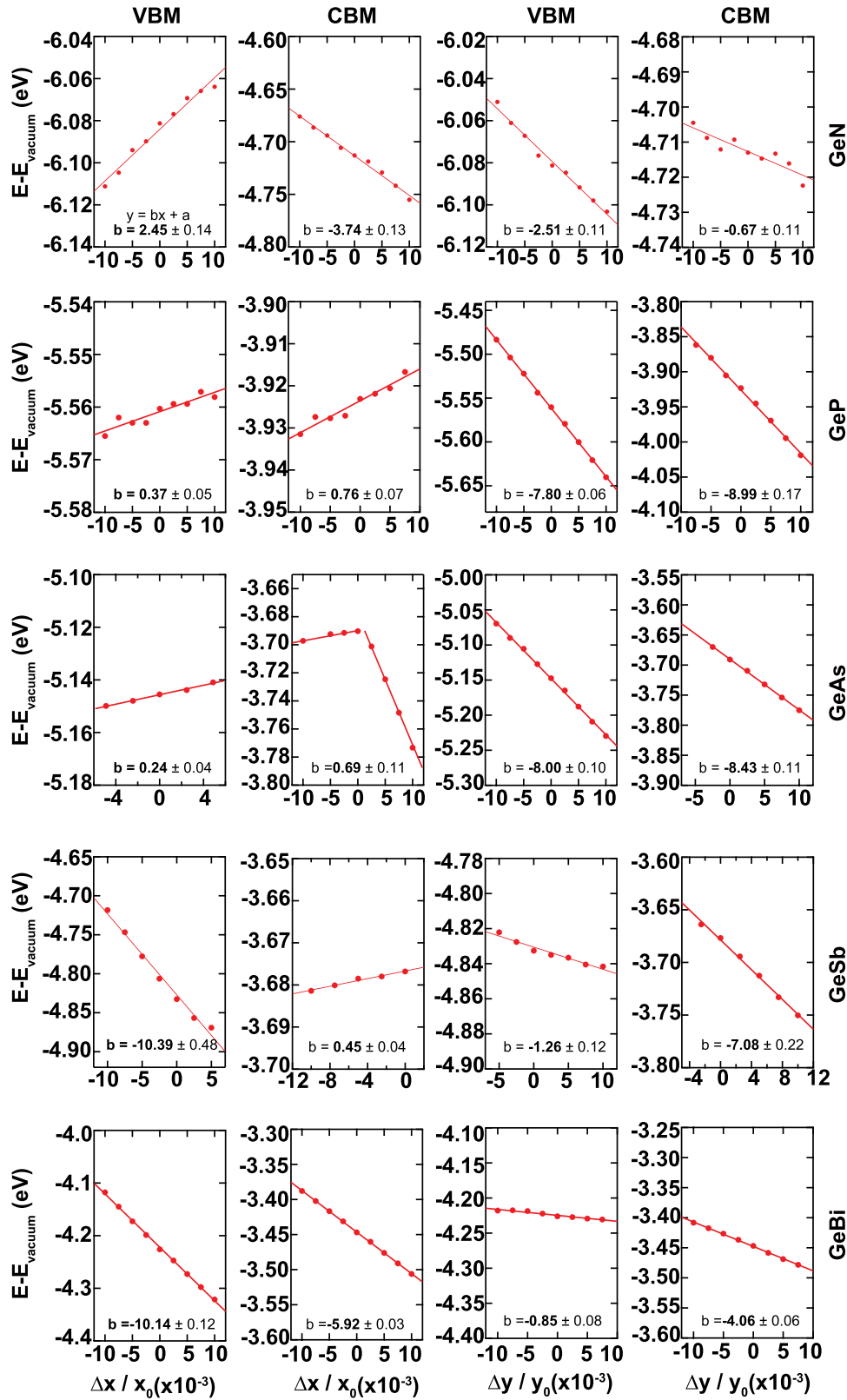
**Figure 9.** Variation of the energy (calculated by the HSE06 functional) of the VBM and CBM with respect to vacuum level as a function of compressive and tensile strain along the transport direction.

J. Phys. D: Appl. Phys. **55** (2022) 185302

M Abboud *et al*

deformation potential constants $E_d$ for different directions and different types of carriers. Once the effective mass of charge carriers and deformation potential constants are obtained, electron and hole mobilities are further predicted along both directions according to the formula:

$$\mu = \frac{e\hbar^3 C_{2D}}{k_B T m^* m_d^* E_d^2}. \tag{4}$$

Here $C_{2D}$ is the elastic constant of corresponding direction, $k_B$ is the Boltzmann's constant, $T$ is the temperature, $m_d^* = \sqrt{m_{ac}^* m_{zz}^*}$ is the density-of-state mass. It should be noted that the equation given above determines the upper value of mobility, taking only electron-phonon coupling into account. The calculated room temperature mobility of electrons and holes in zigzag ($\mu_{e,zz}$, $\mu_{h,zz}$) and armchair ($\mu_{e,ac}$, $\mu_{h,ac}$) directions are given in table 4. In alignment with the effective mass trends, $\mu_{e,zz}$ and $\mu_{h,zz}$ outweigh $\mu_{e,ac}$ and $\mu_{h,ac}$ for almost all structures. The overall anisotropy in charge transport characteristics can be explained by the presence of the $Ge_1-Ge_1$ bonds which makes it difficult for carriers to travel along the armchair direction. For the zigzag direction, conversely, there is an adequate bonding environment that eases the charge carriers' motion throughout this particular direction. Particularly, freestanding GeP and GeSb monolayers have remarkable electron mobilities on the order of $10^5$ cm$^2$ (V s)$^{-1}$, which is much larger than the MoS$_2$ [64]. On the other hand, GeAs and GeP have the highest hole mobility ($\sim 10^5$ cm$^2$ (V s)$^{-1}$) in the zigzag direction with a high degree of anisotropy. Furthermore, GeN has sufficiently high electron mobility ($\sim 10^4$ cm$^2$ (V s)$^{-1}$) in both directions, while it has moderate hole mobility ($\sim 10^3$ cm$^2$ (V s)$^{-1}$) in the zigzag direction and low hole mobility ($180$ cm$^2$ (V s)$^{-1}$) in the armchair direction. Finally, GeBi monolayers also have moderate electron and hole mobilities in both directions.

## 4. Conclusion

In summary, we have systematically investigated structural, mechanical, electronic, and charge carrier transport properties of C2/m-GeX (X = N, P, As, Sb, and Bi) monolayers. AIMD simulations up to 900 K reveal that all the examined 2D crystals are dynamically stable. The mechanical response analysis indicates that studied structures are flexible and demonstrate anisotropic features. Due to its strong covalent bonds, GeN is found to be the stiffest among C2/m-GeX monolayers, and the mechanical strength and rigidity decrease down the X-group. The electronic structure calculations at the level of HSE06 by considering SOC interaction show that all the structures are either direct or quasi-direct semiconductors and their band gaps cover a range from infrared to visible part of the spectrum (0.80–2.37 eV). The inclusion of SOC results in band gap narrowing, and the effect gets stronger as X-atom gets heavier. C2/m-GeX systems have versatile and anisotropic electronic transport features, and among them, particularly GeP and GeAs, possess very high electron and hole mobilities ($\sim 10^5$ cm$^2$ (V s)$^{-1}$) along zigzag direction.

These intriguing properties suggest Ge-pnictogen monolayers as suitable materials for high-performance nanoelectronic devices.

## Data availability statement

The data that support the findings of this study are available upon reasonable request from the authors.

## Acknowledgments

## ORCID iDs

M Abboud  https://orcid.org/0000-0002-6077-8231
D H Ozbey  https://orcid.org/0000-0003-0560-5060
E Durgun  https://orcid.org/0000-0002-0639-5862

## References

[1] Novoselov K S, Geim A K, Morozov S V, Jiang D-E, Zhang Y, Dubonos S V, Grigorieva I V and Firsov A A 2004 *Science* **306** 666
[2] Avouris P, Heinz T F and Low T 2017 *2D Materials* (Cambridge: Cambridge University Press)
[3] Gupta A, Sakthivel T and Seal S 2015 *Prog. Mater. Sci.* **73** 44
[4] Gao E, Lin S-Z, Qin Z, Buehler M J, Feng X-Q and Xu Z 2018 *J. Mech. Phys. Solids* **115** 248
[5] Barreteau C, Michon B, Besnard C and Giannini E 2016 *J. Cryst. Growth* **443** 75
[6] Cheng A-Q, He Z, Zhao J, Zeng H and Chen R-S 2018 *ACS Appl. Mater. Interfaces* **10** 5133
[7] Zacharia R, Ulbricht H and Hertel T 2004 *Phys. Rev.* B **69** 155406
[8] Wang W, Dai S, Li X, Yang J, Srolovitz D J and Zheng Q 2015 *Nat. Commun.* **6** 7853
[9] Li L, Wang W, Gong P, Zhu X, Deng B, Shi X, Gao G, Li H and Zhai T 2018 *Adv. Mater.* **30** 1706771
[10] Jung C S *et al* 2018 *J. Mater. Chem.* A **6** 9089
[11] Kim D *et al* 2019 *J. Mater. Chem.* A **7** 16526
[12] Yang S *et al* 2018 *Adv. Funct. Mater.* **28** 1707379
[13] Sar H, Gao J and Yang X 2020 *Sci. Rep.* **10** 14282
[14] Lee K, Kamali S, Ericsson T, Bellard M and Kovnir K 2016 *Chem. Mater.* **28** 2776
[15] Shen H *et al* 2020 *ACS Appl. Mater. Interfaces* **12** 17466
[16] Nam K-H, Jeon K-J and Park C-M 2019 *Energy Storage Mater.* **17** 78
[17] Shojaei F and Kang H S 2016 *J. Phys. Chem.* C **120** 23842
[18] Grillo A, Di Bartolomeo A, Urban F, Passacantando M, Caridad J M, Sun J and Camilli L 2020 *ACS Appl. Mater. Interfaces* **12** 12998

J. Phys. D: Appl. Phys. **55** (2022) 185302

M Abboud *et al*

[19] Di Bartolomeo A, Grillo A, Giubileo F, Camilli L, Sun J, Capista D and Passacantando M 2020 *J. Phys. D: Appl. Phys.* **54** 105302

[20] Guo J *et al* 2018 *Adv. Mater.* **30** 1705934

[21] Ashton M, Sinnott S B and Hennig R G 2016 *Appl. Phys. Lett.* **109** 192103

[22] Mortazavi B and Rabczuk T 2018 *Physica* E **103** 273

[23] Abboud M, Ozbey D and Durgun E 2021 *Appl. Surf. Sci.* **567** 150793

[24] Matta S K, Zhang C, Jiao Y, O'Mullane A and Du A 2018 *Beilstein J. Nanotechnol.* **9** 1247

[25] Bafekry A, Shojai F, Hoat D M, Shahrokhi M, Ghergherehchi M and Nguyen C 2020 *RSC Adv.* **10** 30398

[26] Lin J-H, Zhang H, Cheng X-L and Miyamoto Y 2017 *Phys. Rev.* B **96** 035438

[27] Meng R, Sun X, Yang D, Bao J and Chen X 2018 *Appl. Mater. Today* **13** 276

[28] Zhou L, Guo Y and Zhao J 2018 *Physica* E **95** 149

[29] Jiao N, Zhou P, He C, He J, Liu X and Sun L 2019 *Phys. Status Solidi* **13** 1900470

[30] Mortazavi B, Shahrokhi M, Cuniberti G and Zhuang X 2019 *Coatings* **9** 522

[31] Gao X, Shen Y, Ma Y, Wu S and Zhou Z 2019 *Inorg. Chem.* **58** 12053

[32] Miao M-S, Botana J, Zurek E, Hu T, Liu J and Yang W 2016 *Chem. Mater.* **28** 1994

[33] Zhang K and Li N 2020 *RSC Adv.* **10** 14225

[34] Ma Z, Zhuang J, Zhang X and Zhou Z 2018 *Front. Phys.* **13** 138104

[35] Feng L, Lu J, Zhang X and Xiang G 2021 *Physica* B **614** 413033

[36] Kresse G and Hafner J 1993 *Phys. Rev.* B **47** 558

[37] Kresse G and Hafner J 1994 *Phys. Rev.* B **49** 14251

[38] Kresse G and Furthmüller J 1996a *Comput. Mater. Sci.* **6** 15

[39] Kresse G and Furthmüller J 1996b *Phys. Rev.* B **54** 11169

[40] Kresse G and Joubert D 1999 *Phys. Rev.* B **59** 1758

[41] Heyd J, Scuseria G E and Ernzerhof M 2003 *J. Chem. Phys.* **118** 8207

[42] Krukau A V, Vydrov O A, Izmaylov A F and Scuseria G E 2006 *J. Chem. Phys.* **125** 224106

[43] Grimme S 2006 *J. Comput. Chem.* **27** 1787

[44] Monkhorst H J and Pack J D 1976 *Phys. Rev.* B **13** 5188

[45] Henkelman G, Arnaldsson A and Jónsson H 2006 *Comput. Mater. Sci.* **36** 354

[46] Mohebpour M A, Mozvashi S M, Vishkayi S I and Tagani M B 2020 *Sci. Rep.* **10** 14963

[47] Özdamar B, Özbal G, Çınar M N, Sevim K, Kurt G, Kaya B and Sevinçli H 2018 *Phys. Rev.* B **98** 045431

[48] Cadelano E, Palla P L, Giordano S and Colombo L 2010 *Phys. Rev.* B **82** 235414

[49] Cooper R C, Lee C, Marianetti C A, Wei X, Hone J and Kysar J W 2013 *Phys. Rev.* B **87** 035423

[50] Zhao H 2012 *Phys. Lett.* A **376** 3546

[51] Peng Q, Wen X and De S 2013 *RSC Adv.* **3** 13772

[52] Qin G and Qin Z 2020 *npj Comput. Mater.* **6** 1

[53] Liu F, Ming P and Li J 2007 *Phys. Rev.* B **76** 064120

[54] Wu J, Wang B, Wei Y, Yang R and Dresselhaus M 2013 *Mater. Res. Lett.* **1** 200

[55] Wang H, Li Q, Gao Y, Miao F, Zhou X-F and Wan X 2016 *New J. Phys.* **18** 073016

[56] Silvi B and Savin A 1994 *Nature* **371** 683

[57] Clements R J, Womack J C and Skylaris C-K 2020 *Electron. Struct.* **2** 027001

[58] Savin A, Jepsen O, Flad J, Andersen O K, Preuss H and von Schnering H G 1992 *Angew. Chem., Int. Ed. Engl.* **31** 187

[59] Lee J, Tian W-C, Wang W-L and Yao D-X 2015 *Sci. Rep.* **5** 11512

[60] Gaddemane G, Vandenberghe W G, Van de Put M L, Chen S, Tiwari S, Chen E and Fischetti M V 2018 *Phys. Rev.* B **98** 115416

[61] Sun J and Leng J 2019 *Phys. Lett.* A **383** 125856

[62] Bardeen J and Shockley W 1950 *Phys. Rev.* **80** 72

[63] Ashcroft N W and Mermin N D 1976 *Solid State Physics* (New York: Holt, Rinehart and Winston)

[64] Radisavljevic B and Kis A 2013 *Nat. Mater.* **12** 815